Imaging the dipole-dipole energy exchange between ultracold rubidium Rydberg atoms

Donald P. Fahey, Thomas J. Carroll, and Michael W. Noel

Phys. Rev. A **91**, 062702 — Published 1 June 2015

DOI: 10.1103/PhysRevA.91.062702

Imaging the dipole-dipole energy exchange between ultracold rubidium Rydberg atoms

Donald P. Fahey,[1] Thomas J. Carroll,[2] and Michael W. Noel[1]
[1]*Physics Department, Bryn Mawr College, Bryn Mawr, PA 19010.*
[2]*Department of Physics and Astronomy, Ursinus College, Collegeville, PA 19426.*

(Dated: May 11, 2015)

The long-range, anisotropic nature of the interaction among atoms in an ultracold dipolar gas leads to a rich array of possibilities for studying many-body physics. In this work, an ultracold gas of highly excited atoms is used to study energy transport due to the long range dipole-dipole interaction. A technique is developed to measure both the internal energy states of the interacting Rydberg atoms and their positions in space. This technique is demonstrated by observing energy exchange between two spatially separated groups of Rydberg atoms excited to two different internal states. Simulations confirm the general features of the energy transport in this system and highlight subtleties associated with the homogeneity of the electric field used in this experiment.

I. INTRODUCTION

How the state of a strongly coupled quantum many-particle system evolves in time is a question which lies at the heart of many molecular, condensed matter, and biological systems. The long range interaction typical in such systems can lead to collective excitation [1], quantum phase transitions [2–4], and evolution governed by complex many-body physics. In recent years, interest has grown in using atoms excited to high electronic energy states, known as Rydberg atoms, to study such phenomena due to their large and exceedingly tunable interactions. In particular, the dipole-dipole interaction usually mediates the dynamics of a gas at ultracold temperatures where collisions are infrequent.

Decades after its initial proposal [5], the goal of engineering simulated quantum many-body systems has seen significant progress [6–8]. Scalable quantum simulators were realized with trapped ions [9–13] and recently, again using ions, it was shown that information propagates at different speeds for systems with long versus short range interactions [14]. In neutral Rydberg atom samples, strongly interacting dissipative systems have been examined [15], while the use of Rydberg excitations for optical spin-waves may lead to scalable quantum information networks or simulations with atoms [16–21]. Laser excitation of an ultracold gas to Rydberg states has led to strongly correlated many-body states, large-scale entanglement, level shifts and the suppression of excitation in nearby ground state atoms [22–26]. Rydberg excitation has been used to demonstrate controlled quantum gate operations in mesoscopic samples [27, 28] and in pairs of individually addressable trapped atoms [29–31]. Recently, coherent energy transport in a chain of three Rydberg atoms was studied as a step toward quantum simulation of spin dynamics [32].

Long-range dipolar interactions have also been studied in degenerate quantum gases such as chromium [33], where an anisotropic deformation of an expanding condensate was seen to depend on the orientation of the atomic magnetic dipole moments, owing to the angular dependence of the dipole-dipole interaction. More recently it was shown that spin relaxation behaviour and spontaneous demagnetization in a chromium condensate are due to resonant dipolar dynamics [34]. Strongly dipolar condensates have recently been created with both erbium [35] and dysprosium [36].

In an ultracold gas, energy can be transferred through the gas on timescales much faster than those over which collisions occur. Energy transport due to many dipole-mediated energy exchange between pairs of Rydberg atoms results in the spatial redistribution of electronic energy states throughout the sample. Field ionization spectroscopy has been used to measure changes in state populations [37] as well as line broadening attributed to many-body interactions [38–40]. Few experiments have been done on the transport of energy in a disordered system with long-range, anisotropic interactions, and it remains to be seen whether phenomena such as localization occur [41, 42].

To study these processes directly, a means of detecting both the internal energy states of interacting Rydberg atoms *and* their positions in space is needed. We demonstrate a technique for doing this that combines selective field ionization with a spatially sensitive electron detector. By adjusting the slew rate and amplitude of an electric field pulse to ionize atoms of only a particular state, and then projecting the resulting electrons onto a spatially sensitive detector in a way that preserves information about their initial positions, we effectively create an image of these states in the sample. By comparison with an image taken at an earlier time the change in the spatial distribution of states is measured and the evolution of resonant energy transfer in the sample can be inferred.

A similar technique, field ionization followed by projection onto a spatially sensitive ion detector, was used to image the spatial correlations that develop during Rydberg state excitation due to an excitation blockade [43, 44]. Field ionization combined with measuring the electron's time of flight has been used to infer spatial information along one dimension [45]. The spatial density distribution of strontium Rydberg atoms has been measured by using a laser to excite a second valence electron, leading to autoionization [46]. The resulting ions are counted and the laser is scanned across the volume of atoms to build up the spatial information. The evolution of an ultracold gas of strontium Rydberg atoms has been imaged by scattering light from core ions [47]. While this technique is not state selective, it could provide insight into the evolution of an ultracold gas into an ultracold plasma. Another optical technique has recently been introduced to image resonant energy transfer in a sample of Rydberg atoms. This technique relies on excitation blockade to shift the Rydberg

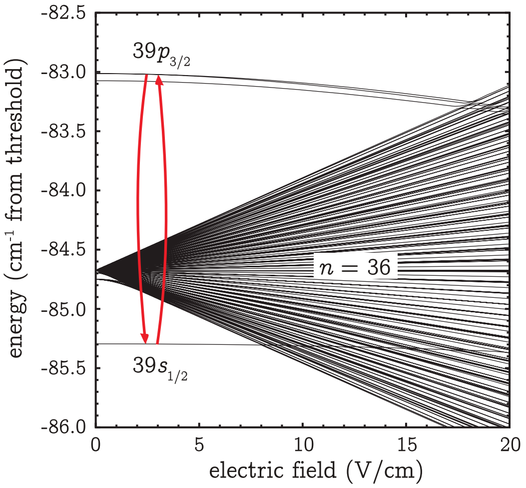

FIG. 1. (Color online) Stark map showing an example of the always resonant energy exchange of Eq. (1) between the $39p_{3/2}$ and the $39s_{1/2}$ states.

states of the dense background of ground state atoms which lie near an excited Rydberg atom [48]. The authors report the observation of the diffusion of impurities in their atomic sample, in agreement with results presented here.

II. EXPERIMENT

As a simple demonstration of our electron imaging technique we excite two parallel cigar-shaped volumes of Rydberg atoms using focused laser beams. The two regions are spaced and oriented so that their volumes, when projected onto the plane of the detector, do not overlap. The lasers are tuned to excite different Rydberg states for each region. Following a short period of interaction, an ionization pulse is applied to detect only atoms in one of the two Rydberg states. The number of these atoms and their positions convey information about the redistribution of energy throughout the sample as a result of dipole-dipole interaction. It is necessary to account for other processes that can cause a change in the electronic energy state of an atom, such as collisions or blackbody radiation induced transitions.

The geometry of our system is similar to the prior work of van Ditzhuijzen *et al.*, in which the authors observe resonant dipole-dipole energy exchange between two spatially resolved parallel cylinders of Rydberg atoms using selective field ionization [49]. The dependence of the energy exchange on the distance between the cylinders and the time evolution of the energy exchange in this system have been studied in experiment and simulation [49, 50]. Our present experiment complements this previous work by imaging the energy transport among the atoms in this geometry.

We use the transition

$$39s_{1/2} + 39p_{3/2} \rightarrow 39p_{3/2} + 39s_{1/2} \qquad (1)$$

depicted in the calculated Stark map of Fig. 1 to realize this technique. The choice of this transition was made for several reasons. At $n = 39$ the difference in neighboring energy states is such that our field ionization pulse can completely resolve the ns and np states. Meanwhile, the sp transition dipole moment is large ($\sim 700ea_0$), thereby increasing the probability of observing resonant energy exchange via the dipole-dipole interaction over very large distances (i.e., tens to hundreds of microns). Because it is always resonant, the interaction scales as $1/R^3$ at zero field and for all electric fields low enough not to cause significant state mixing.

Our experiment measures energy transfer by effectively constraining atoms to two electronic energy states, and then detecting only one of them. Monitoring the change in location of atoms in the detected state can be used to infer the way the atoms interact in the sample. This is valid as long as the total number of atoms in each state is conserved. Here, the field ionization pulse used in detection is set to an amplitude and slew rate such that only atoms in the $39p$ state before the onset of the pulse are ionized. Thus the detection system is only sensitive to the presence of $39p$ atoms.

The choice of the $39s - 39p$ system was also made based on the lack of field tuned resonances. Several field tuned

$$np_{3/2} + np_{3/2} \rightarrow (n-1)s_{1/2} + ns_{1/2} \qquad (2)$$

resonances exist at low field for $n \leq 38$. Were pairs of ns and np states for $n < 39$ to be used, the possibility of inducing pair state transitions through adiabatic rapid passage while the field pulse is ramped to the ionization threshold could cause unwanted changes in the state distribution of the sample.

It is interesting to note that a simple measurement of the final state distribution through selective field ionization, the technique typically used for the measuring field tuned dipole-dipole interaction of Eq. (2) is ineffective for the always resonant exchange of Eq. (1), as the number of atoms in each state is conserved at all times (absent blackbody radiation transitions, spontaneous decay, etc).

The spatially sensitive ion/electron detector used in these experiments was the BOS-18-OPT01 from Beam Imaging Solutions. It consisted of two microchannel plates (MCP) and a phosphor screen assembly housed within a 2.75" conflat flange which was attached to the UHV chamber. The beam of electrons produced from field ionization of the Rydberg sample was imaged through a process of amplification by the MCPs and the conversion of electrons to visible light by a phosphor screen. A triggerable digital camera was used for recording images of the phosphor screen.

The layout of our vacuum system is shown in Fig. 2. The coordinate axes in the center of the figure define directions used for the remainder of our discussion. The x axis coincides with the axis along which the excitation beams propagate. The z axis coincides with the axis of our cylindrical electrodes and detectors.

In the experiment, two side-by-side (separated in the y direction) regions of the cloud of ultracold rubidium atoms in a magneto-optical trap (MOT) were excited to Rydberg states; one to $39p$ and the other to $39s$. This was done by first exciting MOT atoms from $5p_{3/2}$ to $5d_{5/2}$ with a 776 nm diode laser. This beam was weakly focused with a 750 mm focal

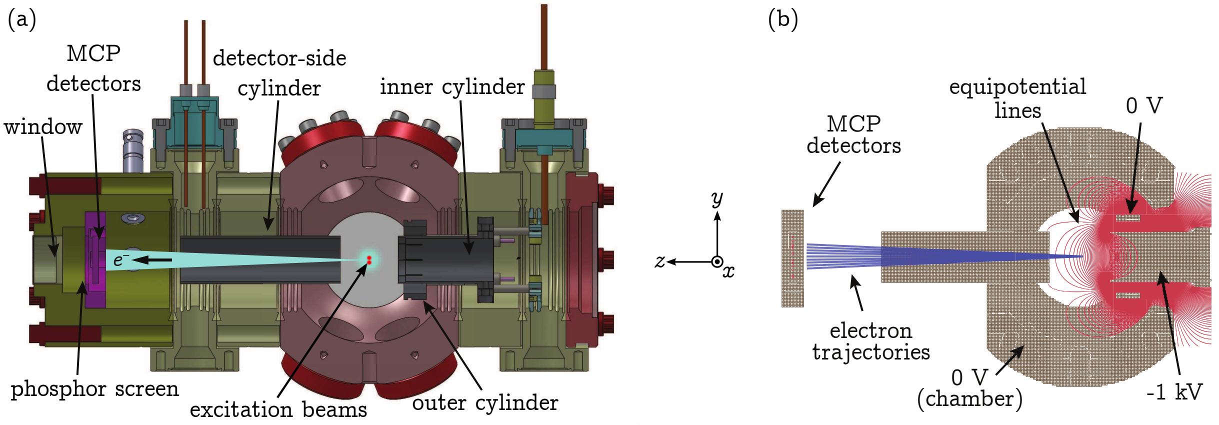

FIG. 2. (color online) (a) A side view of our vacuum chamber. The coordinate axes in the center of the figure define the directions used throughout. The Rydberg excitation beams are propagating into the page in the $-x$ direction and are separated along the y axis. The z direction is along the axis of the cylindrical electrodes, toward the detector. (b) The electron signal is magnified by applying different voltages to the inner and outer cylinders opposite the detector. The red lines indicate equipotentials, while the blue lines represent individual electron trajectories simulated in *SIMION* [51].

length lens onto the densest region of the atom cloud. In addition the $6p_{3/2}$ state was populated throughout via fluorescence from the $5d_{5/2}$ state [52]. A laser beam tuned to the $6p_{3/2} \rightarrow 39s_{1/2}$ transition ($\lambda = 1019.056$ nm) was overlapped with a laser beam tuned to the $5d_{5/2} \rightarrow 39p_{3/2}$ transition ($\lambda = 1265.137$ nm) with a polarizing beam splitter and focused into the MOT with a 100 mm focal length lens from the opposite side so that it was counter-propagating with the 776 nm beam.

The lens used was an achromatic doublet with design wavelengths of 1016 nm, 1330 nm, and 1550 nm, and an antireflection coating for the wavelength range 1050-1620 nm. It was mounted on a pair of translation stages that provided continuous alignment control along the y axis and along the optical axis of the beams (the x axis). Simultaneous adjustment of the horizontal alignment along the z axis for both beams was done with a mirror positioned between the polarizing beam splitter and the lens.

The target shape for the excitation region formed by each laser beam was a long column with a diameter of a few times the inter-Rydberg atomic spacing. To ensure a clean Gaussian profile for the two beams, each was spatially filtered by focusing through a 50 μm diameter pinhole. In each case, the lens used for collimating the beam after the pinhole was selected so that the beam diameter was approximately 1 cm. In the case of the 1265 nm laser, the collimating lens was mounted on a translation stage to allow fine-tuning of the beam divergence. Because a change in the divergence of a beam entering a lens corresponds to a shift in the focal point along the x axis, this made it possible to fine-tune the axial overlap of the foci for the two beams.

The two parallel columns of Rydberg atoms produced by the focused lasers were separated in the y direction along the beams' radial dimension by introducing a small difference in their relative angles prior to the lens. This was accomplished by rotating the beam splitter by a small amount, which modified the angle of the 1265 nm beam only. The distance between the beam splitter and the lens was small enough that these small angular adjustments did not change the position of the 1265 nm beam on the lens significantly.

From the perspective shown in Fig. 2, the excitation beams travel into the page. Given that the detector stack was to the left of the MOT, the phosphor images corresponded to a two-dimensional projection of the excitation volumes in the vertical xy plane orthogonal to the trajectory of the electrons along the z axis. Therefore, the two excitation columns were oriented so that one was above the other along the y axis. Ensuring that the two beams were vertically oriented also meant that the observed distance between the beams in the phosphor images corresponded exactly to the vertical separation along the y axis between the columns in the MOT.

To optimize the axial overlap of the foci in the x direction and to verify that the two beams were aligned in the z direction, a knife edge measurement was performed. A gold plano mirror was inserted between the lens and the vacuum chamber window to reflect the beam at a right angle past a razor blade, through a lens, and onto a photodetector. The razor blade was oriented vertically and mounted on a translation stage, allowing its position to be scanned perpendicular to the beam propagation. The photodetector used for measuring the beam power was sensitive to both wavelengths. The two beams were pulsed and the timing of these pulses was offset, allowing for the simultaneous measurement of both beam's profiles. To sample different regions near the focus, the blade location was fixed and the focus itself was translated by moving the lens. The razor blade was scanned across the beam using a motorized translation stage while the power was measured. Fitting each scan, we extracted the $1/e^2$ radius for each beam. The radii $w(z)$ for a range of locations along the beam axis were fitted to the function

$$w(z) = w_0 \sqrt{1 + \frac{(z - z_0)^2}{z_R}}, \qquad (3)$$

where w_0 gives the 1/e^2 radius at the beam waist, and z_R gives the Rayleigh length (i.e., half of the confocal beam parameter). The z_0 parameter gives the axial position of the focus. If this was found to be different for the two beams, the divergence of the 1265 nm beam was changed slightly and the above process repeated until the foci of the two beams were overlapped. The measured beam waists of ~20 μm agree with the expected diffraction limited spot sizes for the given conditions.

Given that the length scales expected for Rydberg-Rydberg interactions are on the order of tens to hundreds of microns for the densities and Rydberg states examined here, and that the size of the individual MCP channels was 10 μm, some means of magnifying the charge distribution before it arrived at the MCP detectors was needed if significant image distortions were to be avoided. The conducting cylinders that were used to set the electric field in the chamber were designed with this in mind. For all of these experiments, the detector side cylinder was kept at ground or a fixed low voltage (< 10 V). The pair of concentric cylinders opposite the detector could be biased independently. If, in applying the field ionization pulse, the same voltage was applied to both, the field lines seen by the electrons traveling toward the detector were relatively uniform. Some spreading of the charge distribution still occurs due to mutual repulsion of the electrons, but this is small over the very short timescales involved. On the other hand, if the concentric cylinders are biased with opposite polarities the field lines (and thus the electrons) spread out. In this way, a variable magnification of the charge distribution and the phosphor image was achieved.

The program *SIMION* [51] was used to simulate the electron trajectories in our vacuum chamber for a range of cylinder biases. An example image is shown in Fig. 2(b). The red lines depict the equipotentials and the blue lines represent individual electron trajectories. For differently biased cylinders, the curvature of the equipotential lines can be significant, leading to magnification factors in the range of $10^1 - 10^2$ depending on the specific voltages. The symmetry and geometry of the conductors is such that the mapping of the charge distribution at the location of the MOT to the first MCP detector is linear and one-to-one. This assumes that the atoms are initially located along the symmetry axis of the cylinders (the z axis); in other cases, distortions may arise.

While this magnification technique was essential for achieving high-resolution images, it was found to have limitations. The absolute maximum that any image could be magnified was set by the size of the detectors, but loss in quality was usually found before this limit was reached. The system was very sensitive to the location of the atom cloud with respect to the z axis, and transverse displacements of less than 1 mm were enough to cause the electrons to miss the detector. Another area of concern was the reduction in the magnitude of the electric field in the region near the detector due to the spreading of the field lines. If the potential difference between the inner and outer cylinders was made too large, the total energy gained by the electrons on their journey to the detector was too small for them to efficiently trigger a detection event. Thus, a range of differential voltages that were applied to the concentric cylinders was explored to find a compromise between magnification and detection efficiency. A magnification of ~20 provided a good balance and was used for the data presented here. With this magnification the spatial resolution of our detection system was roughly 20 μm. While we did not measure this directly, a typical detection efficiency for a microchannel plate detector is in the range of 50% to 85%.

Because a magnetic field will alter the trajectory of a moving charged particle, the magnetic field for the MOT had to be turned off for the duration of the excitation, interaction, and detection cycle. A power MOSFET was used to shut off the MOT coil current a short time before the beginning of this cycle. Due in part to the inductance of these coils, the magnetic field in the chamber does not go to zero immediately. It was found that 3 ms was a sufficient amount of time to guarantee that the magnetic field was extinguished after the current was turned off. After ionization, the magnetic field was turned back on to reform the trap for the next cycle.

A timing diagram for the experiment is illustrated in Fig. 3(a) along with the excitation scheme for each state in Fig. 3(b). The MOT lasers are left on all the time, but the other excitation lasers are pulsed with acoustic-optic modulators. The 776 nm laser is pulsed on long enough to excite a significant number of atoms to the $5d_{5/2}$, and through fluorescence, the $6p_{3/2}$ states. The 1019 nm and 1265 nm lasers are pulsed for different durations owing to the difference in the efficiency of their excitation schemes. It was found that only 50 ns of 1265 nm light was needed to excite enough atoms to run the experiment. To generate a comparable number of $39s$ atoms, the 1019 nm laser pulse began a few microseconds earlier, and all three were timed to turn off simultaneously. The moment that some atoms were excited to the $39p$ state by the 1265 nm laser pulse, atoms in the sample began to interact and exchange energy. Thus, the start of the interaction time was approximately set by the 1265 nm pulse. The interaction time ended shortly after the start of the field ionization pulse leading to an overall uncertainty in our interaction time of roughly 100 ns. The camera was triggered at the same time as the ionization pulse, and its shutter remained open for 10 μs.

The lasers used to drive each of the transitions shown in Fig. 3(b) were home-built external cavity diode lasers. The MOT lasers were locked to the appropriate transitions in a saturated absorption spectroscopy signal and had a total power of 53 mW for the trapping laser and 30 mW for the repump laser. A MOT temperature of 190 μK was measured using a time of flight technique. The diameter of the atom cloud was roughly 300 μm and we estimate that about 10^7 atoms were trapped, leading to a density of 10^{11}-10^{12} cm^3. The 776 nm laser was locked to a Doppler-free electromagnetically-induced-transparency signal. This was done by overlapping a portion of the beam picked off of the 776 nm laser with a counterpropagating 780 nm beam picked off of the trapping laser in a room temperature rubidium vapor cell and monitoring the transmis-

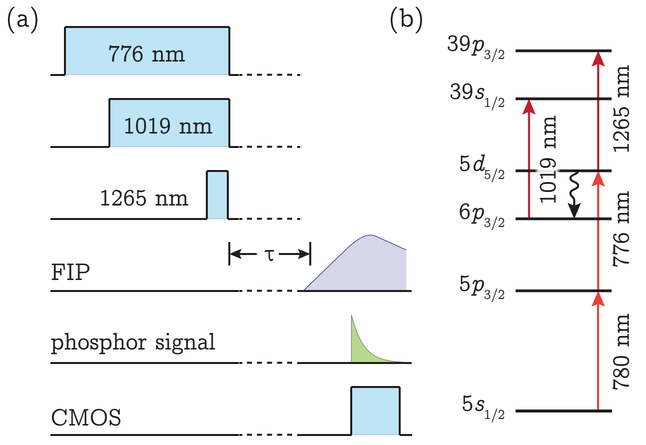

FIG. 3. Timing diagram and excitation scheme for the energy transfer imaging experiments. The atoms are excited by the sequence of pulses in (a) using the excitation scheme shown in (b). The field ionization pulse is triggered after an interaction time τ and is adjusted so that only $39p$ atoms are ionized. The CMOS camera is triggered with an exposure time experimentally adjusted to capture the signal on the phosphor screen. The $39s$ (1019 nm) and $39p$ (1265 nm) excitation pulses are triggered using the scheme shown in Fig. 4.

sion of the 780 nm beam. After locking, 68 mW of power was available in the 776 nm beam. Since we sent the 776 nm beam into the MOT from a single direction, momentum transferred to MOT atoms by photons from this beam was sufficient to push some atoms out of the trap if it was not turned off periodically. To avoid this, we pulsed the 776 nm beam by sending it through an AOM as described earlier. The 1019 nm laser was locked to the side of one of the transmission fringes of a low finesse Fabry-Perot cavity. After locking, spatially filtering, and pulsing a peak power of 12 mW was available for Rydberg state excitation. We locked the 1265 nm laser to an electromagnetically-induced-transparency signal generated by combining it with light from the 780 and 776 nm lasers in a rubidium vapor cell [53]. The peak power available in this laser beam for Rydberg excitation was 7 mW. We do not select a particular m_j sublevel of the $39p_{3/2}$ state.

To calibrate the length scales of the images recorded by this camera, one of the beams was blocked and a transmission diffraction grating was inserted into the unblocked beam immediately before the lens. The result was an image of the far-field diffraction pattern in the focal plane of the lens. Because the light of a collimated laser beam is essentially a monochromatic plane wave, the pattern imaged at the focus consisted of many discrete, parallel beams. Their separation was θf, where θ was the angular separation between neighboring diffracted orders.

The diffraction grating was made by printing an array of parallel lines (0.5 mm thickness, 1 mm separation) on glossy printer paper using a standard laser printer, and then transferring this pattern to a 1” × 3” microscope slide with a hot iron. The Fraunhofer diffraction angle was found by passing the 1019 nm beam through the grating without the lens, and measuring the diffracted order separation at a distance of 2.95 m. This was found to be 2.14 mm. This, together with the lens focal length of 100 mm, gave a separation between the centers of the beams at the focus of 72.5 μm.

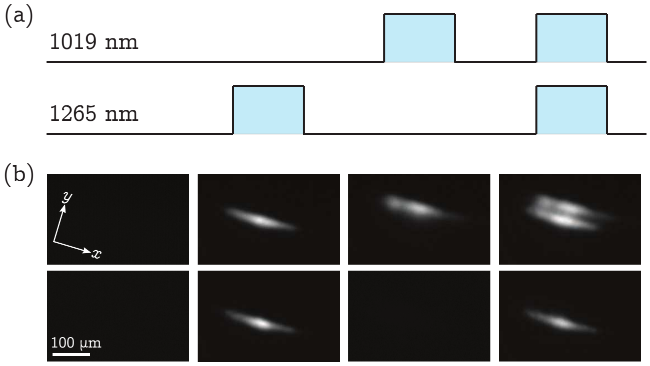

FIG. 4. (a) Pulse sequence for removing background signals due to processes other than resonant energy exchange. The image sequence in the top row of (b) is taken with the field ionization pulse turned up. This allows us to locate the region of Rydberg state excitation for both the $39s$ and $39p$ states. In the bottom row of images in (b), the field ionization pulse is turned down so that only the $39p$ state is ionized. This clearly shows that the field ionization thresholds for the two states are well separated.

The signal current on the phosphor screen was also measured on an oscilloscope. This aided in setting the amplitude of the field ionization pulse so that only the higher energy $39p$ atoms were ionized, while the $39s$ atoms were not. The field ionization spectrum was monitored in real time while the amplitude of the field pulse was lowered until the peak associated with the $39s$ state was no longer visible.

Because the number of $39p$ atoms was used as an indicator of the amount of resonant energy exchange, any non-dipole-dipole interaction processes that result in transitions to or from the $39p$ state must be considered. We accounted for this by collecting data in sets of four images. Only one of these images corresponded to both beams (1019 nm and 1265 nm) being on. The others were taken when only a single beam was on, or neither were on. In the latter cases, all changes in the number of $39p$ atoms must be due to processes other than the dipole-dipole interaction. The image with both beams off was treated as background, and subtracted from the other images. The sum of the two background-free images where only a single beam was on was then subtracted from the background-free image where both beams were on. The resulting image reflects the change in the number of p atoms for each pixel due to having both beams on. The contribution of collisional processes to the signal should be negligible as the microsecond interaction times investigated here are short enough that the Rydberg atoms do not travel an appreciable fraction of their mean interatomic separation.

Care was taken in choosing the order of the images in this sequence. On images where a large signal was observed, there was a risk that the long decay tail of the phosphor could carry over to next image. With the field pulse turned down, two of the four images in the sequence were significantly brighter

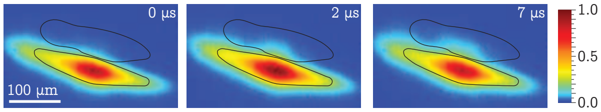

FIG. 5. (Color online) False-color images for different interaction times for the final frame of the sequence shown in Fig. 4(b) (the frame with both beams on, but the field ionization pulse set to only detect 39p atoms). Note the spread of 39p signal into the 39s region (top) for longer interaction times.

than the rest, i.e., those taken when the 39p atoms were excited directly by the 1265 nm laser. The sequence was set such that every other image was bright. This ordering is depicted in Fig. 4(a).

In early experiments it was discovered that this subtraction technique was sensitive enough to be affected by the light that leaked through the AOMs when they were in their "off" state. Specifically, the nonzero extinction of the AOM for the 1265 nm laser resulted in the excitation of a small, but significant, number of 39p state atoms for the frame in the sequence when only 39s atoms were desired. We therefore added mechanical shutters that blocked each beam at the appropriate time in the sequence of frames.

Data was collected for interaction times ranging from ∼100 ns to ∼7.6 μs. The uncertainty in the interaction time is attributed to the with of the 1265 nm pulse, propagation delay in field ionization pulse circuit, and the time taken for the ionization pulse to reach a field where significant state mixing effectively stops the interaction. A gain in the number of 39p atoms in the 39s region should be matched by a similar loss of such atoms in the 39p region of the images. It is unlikely that, after subtraction, changes of this type could be attributed to any process other than the dipole-dipole interaction for these timescales.

The frame sequence in the top row of Fig. 4(b) shows an example phosphor image with the field ionization pulse turned up. This allowed us to locate the region of Rydberg state excitation. The two distinct regions corresponding to the 1019 nm and 1265 nm beams, and thus the regions of 39s and 39p atoms, respectively, are clearly visible. In the bottom row of images in Fig. 4(b), the field ionization pulse is turned down so that only the 39p state is ionized. It is clear from these images that the field ionization thresholds for the two states are well separated.

With the field ionization pulse turned down so that only 39p atoms are ionized, we expect to see changes in the pattern of brightness evolve in time as the atoms resonantly exchange energy. The final frame in the sequence (the frame with both beams on) for three different interaction times is shown in Fig. 5. The interaction times are approximately 0 μs, 2 μs, and 7 μs. Red indicates the presence of 39p atoms, blue indicates the absence of 39p atoms, and the location of the two beams is indicated by a black outline. A change in brightness is clearly seen in the 39s region as the interaction time is lengthened. Each full set of data was collected over the course of 4-8 hours, and typically many hundreds of images were averaged together. Brightness patterns similar those in Fig. 5 were seen for long interaction times on repeated trials of the experiment taken on different days.

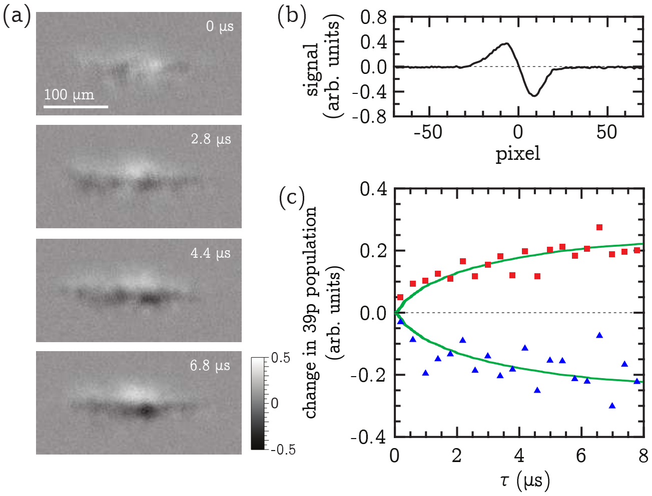

FIG. 6. (Color online) (a) Resonant energy transfer images after subtraction for different interaction times. White indicates an increase in the number of 39p atoms in that region, while black indicates a loss of 39p atoms. (b) A horizontal integration of the subtracted image for an interaction time of 4.4 μs. (c) Change in the number of p state atoms in two equal-area regions of the images. Red squares correspond to a region originally populated by 39s atoms, and blue triangles correspond to a region originally populated by 39p atoms. Simulation results, taken from the same simulations shown in Fig. 8 and Fig. 9, are shown by the solid green line.

Finally, in Fig. 6(a) we show four representative images resulting from the subtraction process described earlier. These images have been rotated so that the two beams appear horizontal. A measure of the total amount of energy exchange was found by integrating these images in the horizontal direction. The result of such an integration is shown in Fig. 6(b). Here a positive signal indicates an increase in the number of 39p atoms while a negative signal indicates a decrease. To find the total number of 39p atoms that have appeared in the region that was originally excited to the 39s state we integrate over the area originally occupied by 39s atoms. An equal area region is integrated to find the total number lost from the region originally excited to the 39p state. This pair of numbers is plotted for each time delay in Fig. 6(c). The increase in 39p state signal in the 39s state region is clearly seen as the interaction time is increased. A corresponding decrease in signal in the 39p state region is also seen, which agrees with the conservation of atom number implicit in the dipole-dipole interaction transition of Eq. (1). The higher noise in the p state region signal may be attributed to detecting a small signal against a large background.

III. MODEL

The data in Fig. 5 show that at successively larger interaction times, 39p character spreads deeper into the 39s region.

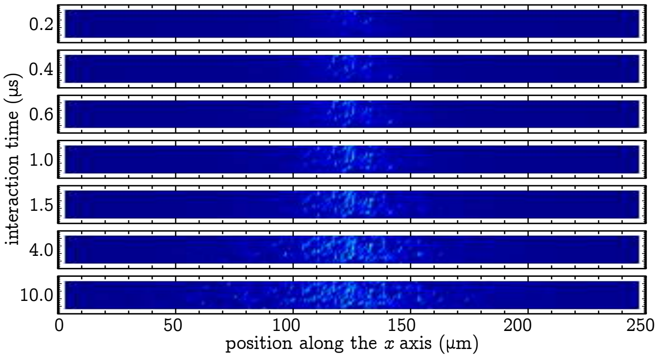

FIG. 7. (Color online) Plot of the change in the number of simulated $39p$ atoms as a function of interaction time and position in a cylindrical volume of length 250 μm which is initially populated with only $39s$ atoms. The radius is 5 μm so the height of each horizontal strip is 10 μm. A small volume of $39p$ atoms is located 5 μm above the center of the $39s$ region but is not shown. The results here are projected into the xy plane just as in the experiment; the y axis is the vertical axis. The results were averaged over thousands of instances with 13-18 s atoms. The color scale is the same as for Fig. 5.

To model this energy transport from the $39p$ region to the $39s$ region, we simulate the energy exchange with a numerical solution of the Schrödinger equation using the full many-body wave function. We ignore radiative decay and blackbody radiation and consider the atoms to be fixed in place, a reasonable assumption given the temperature and time scales in our experiment. Thousands of instances were averaged at discrete time steps (0.05 μs) to compile our results. The simulations were run using both local supercomputing resources and XSEDE [54].

Our simulation includes three Stark states: the $39s_{1/2}$ and both $|m_j|$ sublevels of the $39p_{3/2}$. While we expect the angular dependence of the dipole-dipole interaction to play a role in the spatial evolution of the energy distribution in this system, we did not include the full range of positive and negative m_j values because the additional states would have made the basis so large as to be impractical for even modest numbers of atoms.

We could have further reduced the size of the basis by including only one $39p_{3/2}$ state but we found that including at least two of these states was important for reproducing the dynamics of the energy exchange. Unfortunately, even with only three included Stark states, the size of the basis is too large if physically reasonable numbers of atoms are included in each excitation beam volume. For example, including only 15 atoms in each excitation beam results in more than 10^{12} basis states.

To avoid this problem, we adopted the following strategy. We simulated a smaller region of the two approximately cylindrical excitation volumes and included only 2-4 p atoms with 13-18 s atoms. This allowed us to observe the spread of p character into the s region and generate reasonable statistics since the size of the basis in these cases is $\lesssim 10^5$.

The electric field gradient plays an important role in the time evolution of the energy exchange. Thus we include the curve for each Stark state as a function of applied electric field. Since the electric field is itself a function of position, the energy of each atom will also be a function of the position of that atom. The energy exchange of Eq. (1) is only always resonant if the electric field is homogeneous. In the present case of an inhomogeneous field, atoms at different positions will have different energy gaps between the $39p$ and $39s$ Stark levels and thus be detuned from resonance.

Due to the cylindrical symmetry of our electrode configuration, there are two field gradients: an axial gradient along z axis and a radial gradient perpendicular to that axis. Estimates with SIMION [51] indicate that the axial gradient is an order of magnitude larger than the radial gradient. The axial gradient is perpendicular to the xy plane containing our excitation beams and the radial gradient lies in this plane. This gives different behavior for energy exchange along the excitation volumes (the x axis) as compared to across the excitation volumes (the y axis).

The simpler case is energy exchange along x axis. In this case, the radial gradient will dominate as the length of the excitation volume is much larger than its radius. Thus, to good approximation, the farther apart two atoms are along the excitation volumes the more they will be detuned from resonance. This can be seen in the simulation results of Fig. 7, which shows the probability of detecting a $39p$ atom in the $39s$ region as a function of time and position. We randomly placed $39s$ atoms in a cylinder of length 250 μm and radius 5 μm. We placed a cylinder of length 10 μm and radius 14 μm a distance 5 μm above the center of the $39s$ region and randomly placed $39p$ atoms in it. Just as in the experiment, the cylinder lengths are along the x axis and the cylinders are separated along the y axis. We averaged over thousands of instances with 13-18 $39s$ atoms. Most of the energy exchange occurs in the center, closest to the p region.

The energy exchange across the excitation beams along the y axis is more complex. The radial gradient will tune a pair of atoms out of resonance, while the axial gradient could tune them back into resonance. Since the distances across the beams are similar to the distances within the beams along the z axis, more distant pairs of atoms are not necessarily tuned far out of resonance.

The results of Fig. 7 suggest a strategy for modeling the energy exchange across the beams. Since much of the interaction occurs directly across the two beams, we take a slice across the two beams along the y axis. Fig. 8 shows the results for a simulation in which a 10 μm long slice of a 30 μm radius cylinder is filled with $39s$ atoms. Another cylindrical slice is located 5 μm away and is filled with three $39p$ atoms at similar density. We again averaged over thousands of instances with 13-18 atoms in the $39s$ state. At the earliest times, energy exchange is limited to the parts of the $39s$ region that are closest to the $39p$ region (the "top" in Fig. 8). As time progresses, the $39p$ character diffuses across the beam. Even at later times, there is more $39p$ character at the top, near the $39p$ region.

To more clearly show the spread of p character through the s region, we can use the simulations to view the energy exchange along an axis not available to the experiment. The diffusion is partly obscured in Fig. 8 by the geometric effect

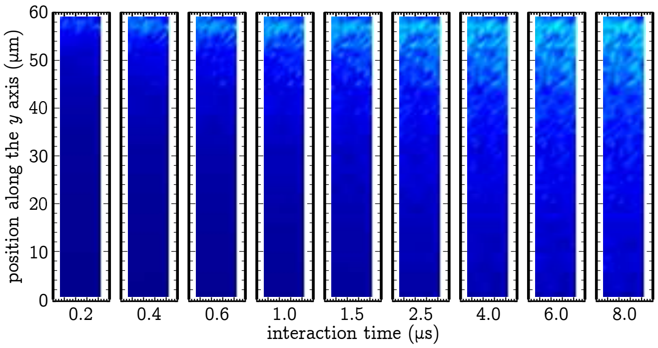

FIG. 8. (Color online) Plot of change in the number of simulated $39p$ atoms as a function of interaction time and position in a slice of a cylindrical volume of length 10 μm and radius 30 μm, which is initially populated with $39s$ atoms. A similar density cylindrical volume of three $39p$ atoms is located 5 μm above the $39s$ region but is not shown. The results here are projected into the xy plane just as in the experiment; the y axis is the vertical axis. The results were averaged over thousands of instances with 13-18 s atoms. The color scale is the same as for Fig. 5.

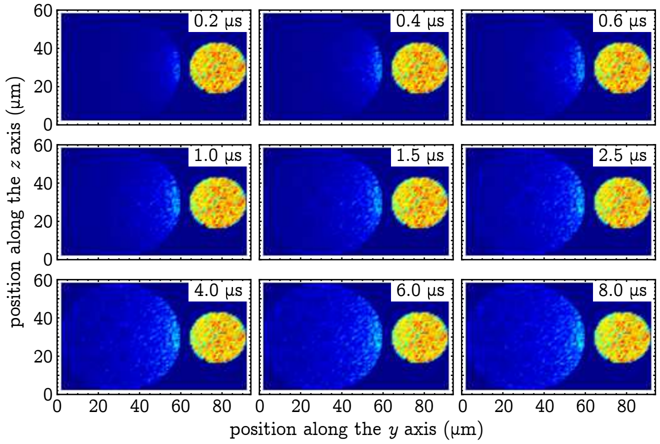

FIG. 9. (Color online) Plot of change in the number of simulated $39p$ atoms as a function of interaction time and position. This is the same data as Fig. 8 but viewed along the excitation beam axis (the x axis). The y axis is the horizontal axis and the z axis is vertical axis. The region initially populated with s atoms in on the left and the p region is on the right. The color scale is the same as for Fig. 5.

of looking through progressively thicker, and thus more populated, regions of the beam. Fig. 9 shows the same results as Fig. 8 but viewed along the x axis. The larger s region is on the left and the smaller p region is on the right. At early times, the p character clearly spreads first to the part of the s region closest to the p region. As time progresses, p character spreads further into the s region.

The simulation results in Figs. 7-9 qualitatively agree with the data in Fig. 5 and Fig. 6. We can also quantitatively compare the simulation results to our data by looking at the time evolution of the change in the $39p$ population. The solid blue lines in Fig. 6(c) show the time evolution predicted by the simulations of Fig. 8 and Fig. 9. The simulation results are scaled vertically since the data in Fig. 6 are not calibrated, but they are not otherwise fit to the data. As can be seen in Fig. 6 there is good quantitative agreement between the data and the predictions of the simulation. The simulations help to elucidate the role of the electric field inhomogeneity and the geometry in the spatial evolution of the energy transport. While the simulations were developed to model this experiment, they will be useful to explore new geometries for future experiments.

IV. CONCLUSION

We have demonstrated that imaging the ionized electrons is a fruitful technique for studying the spatial and temporal evolution of energy transport in a mesoscopic sample of Rydberg atoms. This technique should be broadly applicable as it relies primarily on the well understood process of state selective field ionization. The spatial resolution in our experiments was roughly 20 μm, but can be increased by further magnifying the image. For instance, a resolution of ~0.5 μm was demonstrated in the Rydberg blockade work of Schwarzkopf *et al.* [44]. Detection efficiency is also very good; in the range of 50 to 85% for a typical microchannel plate detector. The time resolution of our system was roughly 100 ns, but again this could be improved by using shorter excitation pulses and a higher slew rate field ionization pulse. However, care must be taken in choosing the slew rate of the field ionization pulse, so that the separation of the states of interest in ionization threshold is still possible. The approach presented here complements the optical imaging work done by Günter *et al.* [48] and is particularly applicable to dilute samples where dipole blockade effects do not play a role.

Imaging techniques like the one demonstrated here provide the opportunity to simultaneously explore the spatial and temporal evolution of quantum dynamics. Recent work has studied the spatial correlations in an amorphous sample of atoms [4, 44]. One could also control the initial spatial arrangement of the sample, as we have in the current experiment by imposing a weak ordering, and then observe the subsequent dynamics. Future imaging experiments could more finely control the initial spatial arrangement of the atoms as well as the Rydberg states to which they are excited. This could be used for quantum simulators, possibly offering insight into solid state systems.

This work was based upon work supported by the National Science Foundation under grant number 1205895. This work used the Extreme Science and Engineering Discovery Environment (XSEDE), which is supported by National Science Foundation grant number ACI-1053575.

---

[1] M. Gärttner, S. Whitlock, D. W. Schönleber, and J. Evers, Phys. Rev. Lett. **113**, 233002 (2014).

[2] G.-B. Jo, Y.-R. Lee, J.-H. Choi, C. A. Christensen, T. H. Kim,

J. H. Thywissen, D. E. Pritchard, and W. Ketterle, Science **325**, 1521 (2009).

[3] R. Islam, E. E. Edwards, K. Kim, S. Korenblit, C. Noh, H. Carmichael, G. D. Lin, L. M. Duan, C. C. Joseph Wang, J. K. Freericks, and C. Monroe, Nat Commun **2**, 377 (2011).

[4] P. Schauß, M. Cheneau, M. Endres, T. Fukuhara, S. Hild, A. Omran, T. Pohl, C. Gross, S. Kuhr, and I. Bloch, Nature **491**, 87 (2012).

[5] R. P. Feynman, Int. J. Theor. Phys. **21**, 467 (1982).

[6] J. I. Cirac and P. Zoller, Nat Phys **8**, 264 (2012).

[7] I. Bloch, J. Dalibard, and S. Nascimbene, Nat Phys **8**, 267 (2012).

[8] I. M. Georgescu, S. Ashhab, and F. Nori, Rev. Mod. Phys. **86**, 153 (2014).

[9] A. Friedenauer, H. Schmitz, J. T. Glueckert, D. Porras, and T. Schaetz, Nat Phys **4**, 757 (2008).

[10] K. Kim, M. S. Chang, S. Korenblit, R. Islam, E. E. Edwards, J. K. Freericks, G. D. Lin, L. M. Duan, and C. Monroe, Nature **465**, 590 (2010).

[11] B. P. Lanyon, C. Hempel, D. Nigg, M. Mueller, R. Gerritsma, F. Zaehringer, P. Schindler, J. T. Barreiro, M. Rambach, G. Kirchmair, M. Hennrich, P. Zoller, R. Blatt, and C. F. Roos, Science **334**, 57 (2011).

[12] J. W. Britton, B. C. Sawyer, A. C. Keith, C. C. J. Wang, J. K. Freericks, H. Uys, M. J. Biercuk, and J. J. Bollinger, Nature **484**, 489 (2012).

[13] Z. Li, H. Zhou, C. Ju, H. Chen, W. Zheng, D. Lu, X. Rong, C. Duan, X. Peng, and J. Du, Phys. Rev. Lett. **112**, 220501 (2014).

[14] P. Richerme, Z.-X. Gong, A. Lee, C. Senko, J. Smith, M. Foss-Feig, S. Michalakis, A. V. Gorshkov, and C. Monroe, Nature **511**, 198 (2014).

[15] N. Malossi, M. M. Valado, S. Scotto, P. Huillery, P. Pillet, D. Ciampini, E. Arimondo, and O. Morsch, Phys. Rev. Lett. **113**, 023006 (2014).

[16] Y. O. Dudin and A. Kuzmich, Science **336**, 887 (2012).

[17] O. Firstenberg, T. Peyronel, Q. Liang, A. V. Gorshkov, M. D. Lukin, and V. Vuletić, Nature **502**, 71 (2013).

[18] D. Maxwell, D. J. Szwer, D. Paredes-Barato, H. Busche, J. D. Pritchard, A. Gauguet, K. J. Weatherill, M. P. A. Jones, and C. S. Adams, Phys. Rev. Lett. **110**, 103001 (2013).

[19] C. S. Hofmann, G. Günter, H. Schempp, M. Robert-de Saint-Vincent, M. Gärttner, J. Evers, S. Whitlock, and M. Weidemüller, Phys. Rev. Lett. **110**, 203601 (2013).

[20] H. Gorniaczyk, C. Tresp, J. Schmidt, H. Fedder, and S. Hofferberth, Phys. Rev. Lett. **113**, 053601 (2014).

[21] D. Tiarks, S. Baur, K. Schneider, S. Dürr, and G. Rempe, Phys. Rev. Lett. **113**, 053602 (2014).

[22] D. Tong, S. M. Farooqi, J. Stanojevic, S. Krishnan, Y. P. Zhang, R. Côté, E. E. Eyler, and P. L. Gould, Phys. Rev. Lett. **93**, 063001 (2004).

[23] K. Singer, M. Reetz-Lamour, T. Amthor, L. G. Marcassa, and M. Weidemüller, Phys. Rev. Lett. **93**, 163001 (2004).

[24] R. Heidemann, U. Raitzsch, V. Bendkowsky, B. Butscher, R. Löw, L. Santos, and T. Pfau, Phys. Rev. Lett. **99**, 163601 (2007).

[25] M. Reetz-Lamour, J. Deiglmayr, T. Amthor, and M. Weidemller, New Journal of Physics **10**, 045026 (2008).

[26] R. Löw, H. Weimer, U. Krohn, R. Heidemann, V. Bendkowsky, B. Butscher, H. P. Büchler, and T. Pfau, Phys. Rev. A **80**, 033422 (2009).

[27] D. Jaksch, J. I. Cirac, P. Zoller, S. L. Rolston, R. Côté, and M. D. Lukin, Phys. Rev. Lett. **85**, 2208 (2000).

[28] L. Isenhower, E. Urban, X. L. Zhang, A. T. Gill, T. Henage, T. A. Johnson, T. G. Walker, and M. Saffman, Phys. Rev. Lett. **104**, 010503 (2010).

[29] H. Labuhn, S. Ravets, D. Barredo, L. Béguin, F. Nogrette, T. Lahaye, and A. Browaeys, Phys. Rev. A **90**, 023415 (2014).

[30] E. Urban, T. A. Johnson, T. Henage, L. Isenhower, D. D. Yavuz, T. G. Walker, and M. Saffman, Nat Phys **5**, 110 (2009).

[31] A. Gaetan, Y. Miroshnychenko, T. Wilk, A. Chotia, M. Viteau, D. Comparat, P. Pillet, A. Browaeys, and P. Grangier, Nat Phys **5**, 115 (2009).

[32] D. Barredo, H. Labuhn, S. Ravets, T. Lahaye, A. Browaeys, and C. S. Adams, Phys. Rev. Lett. **114**, 113002 (2015).

[33] J. Stuhler, A. Griesmaier, T. Koch, M. Fattori, T. Pfau, S. Giovanazzi, P. Pedri, and L. Santos, Phys. Rev. Lett. **95**, 150406 (2005).

[34] M. Fattori, T. Koch, S. Goetz, A. Griesmaier, S. Hensler, J. Stuhler, and T. Pfau, Nat Phys **2**, 765 (2006).

[35] K. Aikawa, A. Frisch, M. Mark, S. Baier, A. Rietzler, R. Grimm, and F. Ferlaino, Phys. Rev. Lett. **108**, 210401 (2012).

[36] M. Lu, N. Q. Burdick, S. H. Youn, and B. L. Lev, Phys. Rev. Lett. **107**, 190401 (2011).

[37] E. Altiere, D. P. Fahey, M. W. Noel, R. J. Smith, and T. J. Carroll, Phys. Rev. A **84**, 053431 (2011).

[38] W. R. Anderson, J. R. Veale, and T. F. Gallagher, Phys. Rev. Lett. **80**, 249 (1998).

[39] I. Mourachko, D. Comparat, F. de Tomasi, A. Fioretti, P. Nosbaum, V. M. Akulin, and P. Pillet, Phys. Rev. Lett. **80**, 253 (1998).

[40] W. R. Anderson, M. P. Robinson, J. D. D. Martin, and T. F. Gallagher, Phys. Rev. A **65**, 063404 (2002).

[41] P. W. Anderson, Phys. Rev. **109**, 1492 (1958).

[42] F. Robicheaux and N. M. Gill, Phys. Rev. A **89**, 053429 (2014).

[43] A. Schwarzkopf, R. E. Sapiro, and G. Raithel, Phys. Rev. Lett. **107**, 103001 (2011).

[44] A. Schwarzkopf, D. A. Anderson, N. Thaicharoen, and G. Raithel, Phys. Rev. A **88**, 061406 (2013).

[45] C. S. van Ditzhuijzen, A. F. Koenderink, L. D. Noordam, and H. van Linden van den Heuvell, The European Physical Journal D - Atomic, Molecular, Optical and Plasma Physics **40**, 13 (2006).

[46] G. Lochead, D. Boddy, D. P. Sadler, C. S. Adams, and M. P. A. Jones, Phys. Rev. A **87**, 053409 (2013).

[47] P. McQuillen, X. Zhang, T. Strickler, F. B. Dunning, and T. C. Killian, Phys. Rev. A **87**, 013407 (2013).

[48] G. Günter, H. Schempp, M. Robert-de-Saint-Vincent, V. Gavryusev, S. Helmrich, C. S. Hofmann, S. Whitlock, and M. Weidemüller, Science **342**, 954 (2013).

[49] C. S. E. van Ditzhuijzen, A. F. Koenderink, J. V. Hernández, F. Robicheaux, L. D. Noordam, and H. B. van Linden van den Heuvell, Phys. Rev. Lett. **100**, 243201 (2008).

[50] T. J. Carroll, C. Daniel, L. Hoover, T. Sidie, and M. W. Noel, Phys. Rev. A **80**, 052712 (2009).

[51] D. Manura and D. Dahl, *SIMION (R) 8.0 User Manual* (Scientific Instrument Services, Inc. Ringoes, NJ 08551, 2008).

[52] D. P. Fahey and M. W. Noel, Opt. Express **19**, 17002 (2011).

[53] P. Thoumany, T. Germann, T. Hänsch, G. Stania, L. Urbonas, and T. Becker, Journal of Modern Optics **56**, 2055 (2009).

[54] J. Towns, T. Cockerill, M. Dahan, I. Foster, K. Gaither, A. Grimshaw, V. Hazlewood, S. Lathrop, D. Lifka, G. D. Peterson, R. Roskies, J. R. Scott, and N. Wilkins-Diehr, Computing in Science & Engineering **16**, 62 (2014).